A Hurricane Morphology and Sea Surface Wind Vector Estimation Model based on C-Band Cross-Polarization SAR Imagery

Guosheng Zhang[1,2], William Perrie[2], Xiaofeng Li [3*], and Jun A. Zhang[4]

[1]International Center for Marine Studies, Shanghai Ocean University, Shanghai, China

[2]Fisheries and Oceans Canada, Bedford Institute of Oceanography, Dartmouth, Nova Scotia, Canada

[3]GST, National Oceanic and Atmospheric Administration (NOAA)/NESDIS, College Park, Maryland 20740, USA

[4]Hurricane Research Division, National Oceanic and Atmospheric Administration (NOAA)/AOML, and Coorperative Institute for Maine and Atmospheric Studies, University of Miami, Miami, Florida, USA

October 2016

Submitted to **IEEE Transactions on Geoscience and Remote Sensing**

*Corresponding Author
Dr. Xiaofeng Li
NOAA/NESDIS
Email: Xiaofeng.Li@noaa.gov

Abstract - Over the last decades, data from spaceborne Synthetic Aperture Radar (SAR) has been used in hurricane research. Some issues remain, for example, when wind is at hurricane strength, the wind speed retrievals from single-polarization SAR suffer from the backscattering signal saturation issue while wind vector retrievals from cross-polarization SAR are not possible due to the fact that the sensitive of backscattering signal in cross-polarization channel to the wind direction change is too low. In this study, we overcome the high-wind retrieval issues by developing a two-dimensional Symmetric Hurricane Estimates for Wind (SHEW) model and combine it with the modified inflow angle model to retrieve wind vector field of a hurricane core structure imaged by cross-polarization SAR. By fitting SHEW to the SAR derived hurricane wind speed, we find the initial closest elliptical-symmetrical wind speed fields, hurricane center location, major and minor axes, the azimuthal (orientation) angle relative to the reference ellipse, and maximum wind speed. This set of hurricane morphology parameters along with the hurricane moving speed are input to the inflow angle model modified with an ellipse-shaped eye to derive the hurricane wind direction. A total of 14 RADARSAT-2 ScanSAR images are employed to tune the combined model and two SAR images acquired over Hurricanes Arthur (2014) and Earl (2010) are used to validate this model. Comparisons between the modeled surface wind vector and measurements from airborne stepped-frequency microwave radiometer (SFMR) and dropwindsondes show excellent agreement. The proposed method works well in areas without significant radar attenuation by precipitation.

Index: Synthetic Aperture Radar, Cross Polarization, Wind, Sea surface electromagnetic scattering

1. INTRODUCTION

Accurate analyses of sea surface wind field, intensity and structure of hurricane or typhoon, all referred to as hurricane hereafter, are critical in enhancing readiness and mitigating risk for coastal communities worldwide. Previous theoretical and numerical studies have tried to understand why and how a hurricane dynamically and thermodynamically forms and how its eye interacts with the eyewall and the circulation in the outer core region [1]-[5]. However, determining the inner core and surface wind field structure of hurricanes remains a considerable operational challenge to the hurricane community [6], even when low-level aircraft reconnaissance data are available. This is in part due to the hurricane wind field is highly azimuthally variable and aircraft typically travel along radial legs at roughly fixed azimuths [7]-[9].

With high spatial resolution, relatively large spatial coverage and capability to image hurricanes on the ocean surface under almost all-weather conditions, spaceborne synthetic aperture radar (SAR) can observe the two-dimensional sea surface wind field. Since the first spaceborne SAR image became available in 1978 [10], hurricanes have been frequently observed by spaceborne SAR images. Over the last few decades, SAR data has been applied in many studies to understand hurricane core characteristics [11] [12], morphology [13]-[15], tracks [16], precipitation [17], and intensity [18] [19]. However, the number of SAR images covering the entire hurricane system was limited until recently when large number of hurricane images was acquired by the RADARSAT, Envisat, and Sentinel-1 SARs [20].

To estimate a complete hurricane core surface wind vector field from a SAR image, a two-dimensional hurricane surface wind estimation model named as Symmetric Hurricane Estimates for Wind (SHEW) model and the inflow angle model have been developed in the literature. The

SHEW model was developed based on three assumptions: 1) the hurricane where the maximum wind speeds occur on an elliptical-shaped eyewall, 2) the radial distribution of the surface wind speeds obeys a continuous analytic function, and 3) the maximum wind speeds on the eyewall are symmetric. The inflow angle model [21], which was originally based on a circular eye, was derived from wind vector observed by over 1600 quality-controlled global positioning system (GPS) dropwindsondes. In this study, we expand the one-dimensional wind profile function to two-dimensional SHEW model and generalize the inflow angle model from a circular eye to an elliptical eye hurricane structure. We then combine the two models to derive the wind vector within hurricane system.

Routinely, a circular hurricane eye was assumed to study the hurricane with along-track observations made by the airborne Stepped Frequency Microwave Radiometer (SFMR) and the Global Positioning System (GPS) dropwindsondes [22]. This circular hurricane eye assumption was used to analyze the hurricane core dynamics, i.e., vortex Rossby wave dynamics [23], the eyewall replacement cycles [4], wind speed asymmetries [24] and hurricane pressure-wind model [9] [25] [26]. Based on the aircraft reconnaissance datasets, a set of continuous analytic functions has been developed [23]. Moreover, the circular eye assumption was also used to SAR images by detecting the wind profile with azimuthal average [19]. Recent research results indicate that most hurricane eye shapes are in the form of circle or ellipse [14], although there is a small portion of hurricane with different shapes of eyes from circle or ellipse [27]. In this study, we combine the elliptical eye shape and the radial continuous analytic function to develop the SHEW model, which is close to the actual hurricane surface wind speed field.

The SHEW model only provides the hurricane surface wind speeds without wind directions. Therefore, the inflow angle model is revised by an elliptical eye assumption to simulate the hurricane wind directions. For hurricane force winds, measurements of the normalized radar cross sections (NRCSs) in VV polarization are generally saturated [28]. Although ocean backscatter from C-band cross-polarized (VH or HV) SAR measurement is quite linear with respect to wind speed, its sensitive to wind direction remains an open question [30, 31]. Therefore, for full wind vector retrieval, we will need to integrate both models.

Following the earlier methodology by [19], the two-dimensional SHEW model is developed. This SHEW model is based on the modified Rankine vortex functions [4] [23] [32] and an elliptical shape for the maximum wind speed contour around the eyewall. When the major axis is equal to the minor axis of the ellipse, it is basically a circle. Additionally, the inflow angle model is extended to simulate surface wind direction by using the parameters of elliptical-eye estimated by SHEW model. The remainder of this paper is organized as follows. The data set is summarized in Section II. Then, we describe the SHEW model and revised inflow angle model in Section III and show the results and validations in Section IV. Conclusions are given in Section V.

II. DATASETS

A. Wide-Swath SAR Data

14 C-band RADARSAT-2 Cross-polarization (VH) ScanSAR wide images covering eleven hurricanes acquired during the Canadian Space Agency (CSA) Hurricane Watch program in 2014 are used to estimate the complete surface wind fields for hurricane core structures. Two additional SAR image over Hurricane Earl (2010) and Hurricane Arthur (2014) were used to validate the developed models. The SAR images are ScanSAR wide swath mode with a medium resolution of 50 m and a swath width of 450 km. We calibrated the SAR image and then averaged the spatial resolution to 1 km with the boxcar averaging method to reduce the image

speckle noise [29]. The 14 hurricane SAR images centered at the eye locations are shown in Figure 1. One can see that some SAR images captured a whole hurricane core, while some only captured part of the hurricane core. Using the cross-polarization SAR wind speed retrieval algorithm, C-band Cross-Polarization Ocean (C-2PO) [30], we can directly derive wind speed from these SAR images.

B. The Stepped-Frequency Microwave Radiometer (SFMR) Data

The stepped-frequency microwave radiometer (SFMR) on board the NOAA (National Oceanic and Atmospheric Administration) WP-3D and U.S. Air Force research aircraft is employed for operational surface wind measurements. It can potentially provide along-track mapping of wind speeds at relatively high spatial (~120 m) and temporal (1 Hz) resolutions. These winds are well validated by measurements from both dropwindsonde and in situ instrument measurements with a RMS error of less than 4 m/s and 5 m/s, respectively [33].

C. Dropwindsonde Data

GPS dropwindsonde data on research and reconnaissance flights is also obtained in this study. Detailed description of dropwindsonde instrumentation and data accuracies can be found in [22]. The near-surface fall speed of a dropwindsonde is about 12-14 m/s, while the typical sampling rate is 2 Hz, yielding an approximately 5-7 m vertical sampling. Note that the 5-s filter, which is typically applied in the postprocessing, effectively reduces the vertical resolution to roughly an order of magnitude lower than the original sampling. The accuracy of the horizontal wind speed measurements is on the order of 0.5 m/s. The dropwindsonde data obtained after 2005 have been postprocessed using the National Center for Atmospheric Research Atmospheric Sounding Processing Environment (ASPEN) software. Recent studies have indicated little difference between winds processed by different processing systems [34]. To validate the hurricane surface wind vector estimated by the combination of SHEW and revised inflow angle models, the dropwindsonde datasets during 6 hours (UTC) of the SAR image were employed.

III. HURRICANE WIND RETRIEVAL METHODOLOGY

A. The Hurricane SHEW Model

Applying the C-2PO wind speed retrieval model to the 14 cross-pol SAR images covering part or whole of the hurricane core, the radial distributions of surface wind speeds during 150 km are displayed in Figure 2 as well as the mean wind profile. All 14 SAR images were taken in a relatively weak hurricane-vortex with maximum axisymmetric wind speed on order of 25 - 35 m/s. The averaged radial wind profile in red represents the axisymmetric wind structure, while the variance in radial wind profile represents the azimuthal variations. The radii of the maximum wind speed (RMWs) in every 5^{o} azimuth angle are displayed in Figure 3, indicating that the shapes of most cases are close to ellipses. Therefore, if an elliptical-shaped eye is adapted to continuous analytic function, a two dimensional analytic model may be developed to estimate the main structure of the hurricane eye shape (circle or ellipse). For the surface structure of a hurricane, the symmetry is normally referred to rotational symmetry [14]. In contrast with previous studies, the symmetry in the SHEW model is noted as elliptical symmetry which is a reflectional but not rotational symmetry. Therefore, the two dimensional RMWs are built in terms of the major and the minor axis of an ellipse as:

$$r_m(\theta) = a \cdot b / \sqrt{(b \cdot cos\theta)^2 + (a \cdot sin\theta)^2} \quad (1)$$

where a is the major axis, b is the minor axis, both with units of km, and θ is the angle respect to the major axis. With this reference ellipse formulation, the one-dimensional continuous analytic functions are extended to two-dimensions. The surface wind field for an elliptical vortex is:

$$V(r,\theta) = \begin{cases} V_{max} * \left[\frac{r}{r_m(\theta)}\right], & \left(r \le r_m(\theta)\right) \\ V_{max} * \left[\frac{r_m(\theta)}{r}\right]^{\alpha}, & (r_m(\theta) < r \le 150 \text{ km}) \end{cases} \quad (2)$$

where α is the decay parameter, r is the radial distance to the hurricane center with the unit of km, and V_{max} is the maximum wind speed on the assumed elliptical eyewall. In (2), the wind speed for an elliptical symmetrical hurricane with one vortex can be reconstructed for given reference ellipse parameters of a and b, as well as the intensity parameters of V_{max} and α. For example, assuming a major axis of 25 km, a minor axis of 20 km, a maximum wind speed of 30 m/s, and a decay parameter of 0.5, the elliptical symmetric wind field constructed by the SHEW model is shown in Figure 4.

B. The Revised Inflow Angle Model

In the original inflow angle model [21], the radial distances are normalized by the axisymmetric RMW ($r^*=r/r_m$) assuming the eye and eyewall has a circle shape. For the elliptical-shaped eyewall, it is revised as:

$$r^*(\theta) = \frac{r}{r_m(\theta)} \quad (3)$$

By inputting the hurricane motion speed as well as three morphology parameters (a, b & V_{max}) to the revised model, the inflow angle in a hurricane can be constructed. In this study, the morphology parameters are detected by fitting SHEW model to the wind speed field retrieved from SAR image. For example, assuming hurricane motion speed of 2m/s, a major axis of 25 km, a minor axis of 20 km, and a maximum wind speed of 30 m/s, the inflow angle field and wind vector constructed by the revised model are shown in Figure 5.

C. Hurricane Surface Wind Vector Estimation Procedure

The flowchart shown in Figure 6, demonstrates the procedures of using the SHEW and revised Inflow Angle models to estimate the completed hurricane surface wind vector from the C-band cross-polarized SAR image. When the hurricane morphology parameters with the elliptical eye are inputted to the SHEW model, a wind speed field can be estimated. At the same time, the inflow angle structure is estimated with a given hurricane motion speed. Then, a wind vector field can be calculated with the wind speed from SHEW model and the wind direction from the revised inflow angle model. By comparing with the wind speed retrieved from the VH-polarized SAR image based on the C-2PO algorithm, the closet surface wind vector field is estimated with the least squares methodology. Finally, the hurricane surface wind vector field is validated by aircraft measurements (SFMR and dropwindsonde). To simplify this process, an initialized wind field were firstly retrieved from cross-polarized SAR image using the C-2PO algorithm. Secondly, SHEW model was fit to the initialized wind. And then the wind directions were simulated by providing the maximum wind speed and reference ellipse estimated by SHEW model as well as the hurricane motion speed to the revised inflow angle model.

By fitting the SHEW model to the VH-polarized SAR image, the closest elliptical symmetrical wind speed fields for the 14 SAR images in the year of 2014 are detected (Figure 7). The RMSEs and correlation coefficients between the elliptical symmetrical wind fields and C-2PO retrieved wind fields for the 14 cases are shown in Figure 8. The RMSEs are less than 4m/s. The correlations are higher than 60%, except for the first SAR image for hurricane Vance (only 21.3%). The hurricane morphology and intensity parameters were detected from the 14 SAR images by SHEW model (Table I). Moreover, the hurricane elliptical morphology parameters of the closet wind speed field were detected. Of note, the reason for the low correlation of the first image for Hurricane Vance will be further studied in the future.

By providing the maximum wind speed and reference ellipse estimated by SHEW model as well as the hurricane motion speed by the Best Track data (HURDAT2) from National Hurricane

Center (http://www.nhc.noaa.gov/data/), the 2D surface inflow angles for the 14 SAR images are estimated and shown in Figure 9. Then the complete surface wind vector fields for the hurricanes acquired by the SAR images are estimated (Figure 10), based on the wind directions estimated by the revised inflow angle and the wind speeds estimated by SHEW model.

IV. SAR WIND VECTOR VALIDATION AGAINST AIRCRAFT MEASUREMENTS

The SFMR dataset is used to validate the symmetric wind speed fields estimated by SHEW model, and the dropwindsonde dataset is usedto validate the wind vector derived by the combined SHEW and inflow angle models (as shown in Figure 6). Two SAR cases were matched up with aircraft datasets: Hurricane Arthur (2014) and Hurricane Earl (2010).

For Hurricane Arthur, one radial profile in the radius of 150 km was fully observed by the SFMR within a 10 minute time window when the SAR image was acquired. The SAR image acquired at 11:14 UTC (3 July 2014) for Hurricane Arthur, locations of matched SFMR data (during 11:04 to 11:27 UTC, 3 July 2014) are shown in Figure 11a. In this study, we assume the hurricane structure remains stable and does not change much during the period of interest. Then, the storm-relative locations are detected by removing the physical radial locations of observations from the hurricane center location calculated based on the linearly interpolated Best Track data. The storm-relative locations of the dropwindsonde data are also shown in Figure 11a.

The radial wind profiles observed by the SFMR and estimated by the SHEW model respect to the SFMR locations are shown in Figure 12a. Of note, more than half of the SFMR locations are outside the SAR image as it only captured part of the hurricane core structure. From the wind profiles, the maximum wind speed estimated by the SHEW model is 28.7 m/s, which is close to the observed value of 27.6 m/s by the SFMR. The corresponding RMWs are 31 km and 29 km, respectively, for the SHEW and SFMR. The radial wind profile estimated by the SHEW model is found to be close to that observed by SFMR even when there is no SAR data, showing robustness of the SHEW model for 2D wind speed estimation. To validate the wind direction estimates, we calculated the wind vector (decomposed in zonal and meridional components) by using the wind speed estimated by the SHEW model and wind direction estimated by revised inflow angle model. The wind vectors estimated by the two models and observed by dropwindsondes are shown in Figure 13a, which demonstrates good agreement between the model and observation. The statistics in terms of RMSE, bias and correlation coefficients suggests that the combined SHEW and inflow angle model excellently captured the observed wind vector distribution in both storms. This also demonstrates the ability for this combined model to accurately estimate the complete hurricane surface wind fields when a SAR image only covers a large portion of the hurricane core region. This capability is beyond the standard C-2PO algorithm.

To further validate our models, the SAR image for Hurricane Earl (22:59 UTC, September 2, 2010) is acquired (Figure 11b), which captured a complete hurricane core. However, wind speeds retrieved from SAR image are underestimated due to heavy rainfall (Figure 12b). As we learned from our previous study [17], heavy rain associated with the hurricane attenuates the radar signal of SAR. As seen in Figure 12b, coinciding with the heavy rain region, an obvious moat exists in the SAR wind profile derived by the C-2PO algorithm. Although the SHEW-estimated wind profile is also somewhat different from the SFMR-observed one, it is much better than the C-2PO retrieved wind profile. The local effects due to the attenuation by rain could be reduced by adopting the SHEW model. This reduction may be a result that SHEW model is fitted to all the azimuth angles while the rain band with heavy rainfall only exists at certain azimuth angles at the same radius. Therefore, the wind profile (red line in Figure 12b) estimated by SHEW model which was fitted to all azimuth angles is closer to the SFMR wind profile than that retrieved from SAR image directly. Moreover, the wind vectors estimated by the combined models are validated by using the collocated dropwindsondes (Figure 13b) for Hurricane Earl (2010), showing very good agreement (see statistics in Table 2).

V. CONCLUSIONS

To estimate a complete wind vector field from a cross-polarized SAR image, two-dimensional SHEW model is developed and the inflow angle model is revised both based on an assumption of an elliptical shaped eye and eyewall. In the SHEW model, we assume an elliptical eyewall shape where the maximum wind speeds exist, as a generalization of the one-dimensional wind profile in each radial direction. When the SHEW model was applied to C-band RADARSAT-2 cross-polarized SAR images, the elliptical symmetrical wind speed field can be estimated and morphology parameters and intensity parameter can be detected. To simulate the wind direction for cross-polarized SAR images, the inflow angle model is revised by adopting an ellipse-shaped eye to replace the former circular-shaped eye. By providing the morphology parameters estimated by SHEW model and the hurricane motion vector from the Best Track data, the wind direction can be estimated by the revised inflow angle model. Combining the wind speed by SHEW and wind direction by revised inflow angle model, the complete surface wind vector field of a hurricane is estimated from the SAR image. For 14 SAR images of hurricane observed in 2014, the closest elliptical symmetrical surface wind speed fields and surface wind vector fields were estimated, with six elliptical morphology parameters: hurricane centers, reference ellipse parameters (major axis, minor axis, and azimuth angle), hurricane symmetric intensity and decay parameter. Comparisons between the wind vectors based on our model and observations show good agreement. Additionally, the influence due to the attenuation by heavy rain is declined, when the SHEW model is applied to the SAR images to retrieve wind speed.

There are three possible problems recognized when we process C-band cross-polarized SAR images: (1) many SAR images capture incomplete hurricane core structures; (2) the radar signal is attenuated by the heavy precipitation associated with hurricane; (3) wind directions are hard retrieve from the measurements cross-polarized SAR images, although cross-polarization appears to not saturate and linear respect to sea surface wind speed.

Of note, although our models capture the main features of a hurricane eye shape, there is still a good amount of unexplained variability which requires further study. To simplify the problem, the SAR images analyzed in this study are from weak storms with barely Category 1 hurricane strength. The distribution of wind speeds estimated by SHEW model is an idealized and elliptical-shaped structure. The wind speeds retrieved from SAR image by using C-2PO model are expected as the real wind speeds. Therefore, if the correlation between the two sets of wind speeds is high, the real hurricane structure is close to an idealized one. Therefore, we draw the conclusion that the storm captured by the first Hurricane Vance image did not behave as well as the others did. Moreover, the reason for why the first Hurricane Vance storm behaves differently from the others will be further studied.

Acknowledgements

The authors would like to thank the Canadian Space Agency for providing RADARSAT-2 dual-polarization SAR images, the NOAA Hurricane Research Division, NOAA Aircraft Operations Center and US Air Force for collecting and maintaining the SFMR and dropsonde data. The views, opinions, and findings contained in this report are those of the authors and should not be construed as an official NOAA or U.S. government position, policy, or decision.

References

[1] R. K. Smith, “Tropical cyclone eye dynamics,” *J. Atmos. Sci.*, vol. 37, no. 6, pp. 1227–1232, Feb. 1980, doi: 10.1175/1520-0469(1980)037<1227:TCED>2.0.CO;2.

[2] L. J. Shapiro and H. E. Willoughby, “The response of balanced hurricanes to local sources of heat and momentum,” *J. Atmos. Sci.*, vol. 39, no. 2, pp.378-394, 1982, doi: 10.1175/1520-0469(1982)039<0378:TROBHT>2.0.CO;2.

[3] H. E. Willoughby, “Temporal changes of the primary circulation in tropical cyclones,” *J. Atmos. Sci.*, vol. 47, no. 2, pp. 242-264, 1990, doi: 10.1175/1520-0469(1990)047<0242:TCOTPC>2.0.CO;2.

[4] M. Sitkowski, J. P. Kossin, and C. M. Rozoff, “Intensity and structure changes during hurricane eyewall replacement cycles,” *Mon. Weather Rev.*, vol. 139, no. 12, pp. 3829-3847, Apr. 2011, doi: 10.1175/MWR-D-11-00034.1.

[5] Z. Zhu and P. Zhu, “Sensitivities of eyewall replacement cycle to model physics, vortex structure, and background winds in numerical simulations of tropical cyclones,” *J. Geophy. Res.*, vol. 120, no. 2, pp. 590-622, Jan. 2015, doi: 10.1002/2014JD022056.

[6] E. R. Sanabia, B. S. Barrett, N. P. Celone, and Z. D. Cornelius, “Satellite and Aircraft Observations of the Eyewall Replacement Cycle in Typhoon Sinlaku (2008),” *Mon. Weather Rev.*, vol. 143, no. 9, pp. 3406-3420, May 2015, doi: 10.1175/MWR-D-15-0066.1.

[7] J. P. Kossin and M. D. Eastin, “Two distinct regimes in the kinematic and thermodynamic structure of the hurricane eye and eyewall,” *J. Atmos. Sci.*, vol. 58, pp. 1079–1090, May 2001, doi: 10.1175/1520-0469(2001)058,1079:TDRITK.2.0.CO;2.

[8] J. L. Franklin, M. L. Black, and K. Valde, “GPS dropwindsonde wind profiles in hurricanes and their operational implications,” *Weather Forecast.*, vol. 18, pp. 32-44, Feb. 2003, doi: 10.1175/1520-0434(2003)018<0032:GDWPIH>2.0.CO;2.

[9] J. P. Kossin, “Hurricane Wind–Pressure Relationship and Eyewall Replacement Cycles,” *Weather Forecast.*, vol. 30, no. 1, pp. 177-181, Feb. 2015, doi: 10.1175/WAF-D-14-00121.1.

[10] L. L. Fu and B. Holt, “Seasat views oceans and sea ice with synthetic aperture radar,” Feb. 1982.

[11] Y. Du and P. W. Vachon, “Characterization of hurricane eyes in RADARSAT-1 images with wavelet analysis,” *Can. J. Remote Sens.*, vol. 29, no. 4, pp. 491-498, Jun. 2003, doi: 10.5589/m03-020.

[12] S. Jin, S. Wang, and X. Li, “Typhoon eye extraction with an automatic SAR image segmentation method,” *Int. J. Remote Sens.*, vol. 35, no. 11–12, pp. 3978-3993, Dec. 2014, doi: 10.1080/01431161.2014.916447.

[13] K. Friedman and X. Li, “Storm patterns over the ocean with wide swath SAR,” *Johns Hopkins Univ. APL Tech. Dig*, vol. 21, pp. 80-85, 2000.

[14] X. Li, J. A. Zhang, X. Yang, W. G. Pichel, M. DeMaria, D. Long and Z. Li, "Tropical cyclone morphology from spaceborne synthetic aperture radar," *Bull. Amer. Meteor. Soc.*, vol. 94, no. 2, pp. 215-230, Feb. 2013.

[15] I. Lee, A. Shamsoddini, X. Li, J. C. Trinder, and Z. Li, "Extracting hurricane eye morphology from spaceborne SAR images using morphological analysis," *ISPRS J. Photogramm.*, vol. 7, pp. 115-125, 2016, doi: 10.1016/j.isprsjprs.2016.03.020.

[16] G. Zheng, J. Yang, A. K. Liu, X. Li, W. G. Pichel, and S. He, "Comparison of typhoon centers from SAR and IR Images and those from best track datasets," *IEEE Trans. Geosci. Remote Sens.*, vol. 54, no. 2, pp. 1000-1012, 2016, doi:10.1109/TGRS.2015.2472282.

[17] G. Zhang, X. Li, W. Perrie, B. Zhang, and L. Wang, "Rain effects on the hurricane observations over the ocean by C-band Synthetic Aperture Radar," *J. Geophy. Res.*, vol. 121, no. 1, pp. 14-26, Jan. 2016, doi: 10.1002/2015JC011044.

[18] A. Reppucci, S. Lehner, J. Schulz-Stellenfleth, and S. Brusch, "Tropical cyclone intensity estimated from wide-swath SAR images," *IEEE T. Geosci. Remote S.*, vol. 48, no. 4, pp. 1639-1649, Feb. 2010, doi: 10.1109/TGRS.2009.2037143.

[19] G. Zhang, B. Zhang, W. Perrie, Q. Xu, and Y. He, "A Hurricane Tangential Wind Profile Estimation Method for C-Band Cross-Polarization SAR," *IEEE Trans. Geosci. Remote Sens.*, vol. 52, no. 11, pp. 7186-7194, Apr. 2014, doi: 10.1109/TGRS.2014.2308839.

[20] X. Li, "The First Sentinel-1 SAR Image of a Typhoon," *Acta. Oceanol. Sin.*, vol. 34, no. 1, pp. 1-2, Jan. 2015, doi: 10.1007/s13131- 015-0589-8.

[21] J. A. Zhang and E. W. Uhlhorn, "Hurricane sea surface inflow angle and an observation-based parametric model," *Mon. Weather Rev.*, vol. 140, no. 11, pp. 3587-3605, May 2012, doi: 10.1175/MWR-D-11-00339.1.

[22] T. F., Hock and J. L. Franklin, "The ncar gps dropwindsonde," *Bull. Amer. Meteor. Soc.*, vol. 80, no. 3, pp. 407-420, Mar. 1999, doi: 10.1175/1520-0477(1999)080<0407:TNGD>2.0.CO;2.

[23] K. J. Mallen, M. T. Montgomery, and B. Wang, "Reexamining the near-core radial structure of the tropical cyclone primary circulation: Implications for vortex resiliency," *J. Atmos. Sci.*, vol. 62, no. 2, pp. 408-425, Feb. 2005, doi: 10.1175/JAS-3377.1.

[24] E. W. Uhlhorn, B. W. Klotz, T. Vukicevic, P. D. Reasor, and R. F. Rogers, "Observed hurricane wind speed asymmetries and relationships to motion and environmental shear," *Mon. Weather Rev.*, vol. 142, no. 3, pp. 1290-1311, Mar. 2014, doi: 10.1175/MWR-D-13-00249.1.

[25] G. Holland, "A revised hurricane pressure-wind model," *Mon. Weather Rev.*, vol. 136, no. 9, pp. 3432-3445, 2008, doi: 10.1175/2008MWR2395.1.

[26] G. J. Holland, J. I. Belanger, and A. Fritz, "A revised model for radial profiles of hurricane winds," *Mon. Weather Rev.*, vol. 138, no. 12, pp. 4393-4401, Dec. 2010, doi: 10.1175/2010MWR3317.1.

[27] P. D. Reasor, M. T. Montgomery, F. D. Marks Jr., and J. F. Gamache, "Low-wavenumber structure and evolution of the hurricane inner core observed by airborne dual-Doppler radar,"

Mon. Wea. Rev., vol. 128, pp. 1653–1680. Jun. 2000, doi: 10.1175/1520-0493(2000)128<1653:LWSAEO>2.0.CO;2.

[28] D. E. Fernandez, J. R. Carswell, S. Frasier, P. S. Chang, P. G. Black, and F. D. Marks, "Dual-polarized C-and Ku-band ocean backscatter response to hurricane-force winds," *J. Geophy. Res.*, vol. 111, no. C8, Aug. 2006, doi: 10.1029/2005JC003048.

[29] H. Shen, W. Perrie, Y. He, and G. Liu, "Wind Speed Retrieval From VH Dual-Polarization RADARSAT-2 SAR Images," *IEEE Trans. Geosci. Remote Sens.*, vol. 52, no. 9, pp. 5820-5826, May 2014, doi: 10.1109/TGRS.2013.2293143.

[30] B. Zhang and W. Perrie, "Cross-polarized synthetic aperture radar: A new potential measurement technique for hurricanes," *Bull. Amer. Meteor. Soc.*, vol. 93, no. 4, pp. 531-541, Apr. 2012, doi: http://dx.doi.org/10.1175/BAMS-D-11-00001.1.

[31] J. Horstmann, S. Falchetti, C. Wackerman, S. Maresca, M. J. Caruso, and H. C. Graber, "Tropical Cyclone Winds Retrieved From C-Band Cross-Polarized Synthetic Aperture Radar," *IEEE Trans. Geosci. Remote Sens.*, vol. 53, no. 5, pp. 2887-2898, Jan. 2015, doi: 10.1109/TGRS.2014.2366433.

[32] V. T. Wood, L. W. White, H. E. Willoughby, and D. P. Jorgensen, "A new parametric tropical cyclone tangential wind profile model," *Mon. Wea. Rev.*, vol. 141, no. 6, pp. 1884-1909, Jun. 2013, doi: 10.1175/MWR-D-12-00115.1.

[33] E. W. Uhlhorn and P. G. Black, "Verification of remotely sensed sea surface winds in hurricanes," *J. Atmos. Ocean. Tech.*, vol. 20, no. 1, pp. 99-116, Jan. 2003, doi: 10.1175/1520-0426(2003)020<0099:VORSSS>2.0.CO;2.

[34] G. M. Barnes, “Atypical thermodynamic profiles in hurricanes,” *Mon. Wea. Rev.*, vol. 136, pp. 631–643, Feb. 2008, doi: 10.1175/2007MWR2033.1.

Table I. hurricane morphology and intensity estimated by the SHEW model applied to 14 SAR images

Hurricane name	Date(yy-mm-dd)	Time (UTC)	hurricane center		Reference Ellipse			Intensity	
			latitude	longitude	Major (Km)	Minor (Km)	Azimuth	u_m (m/s)	α
Ana	14-10-19	04:45	19.98°N	159.29°W	27.1	22.1	157°	28.6	0.45
Cristina	14-06-15	13:23	20.03°N	113.12°W	57.9	41.9	80°	17.1	0.71
Rammasun	14-07-17	10:28	17.36°N	114.52°E	32.3	28.3	7°	35.0	0.35
Iselle	14-08-03	14:35	15.53°N	132.57°W	22.5	18.5	64°	33.2	0.42
	14-08-07	15:59	18.63°N	150.99°W	26.7	24.7	143°	27.4	0.30
Karina	14-08-14	01:47	17.03°N	113.65°W	27.2	24.2	79°	27.7	0.56
Norbert	14-09-07	01:50	25.48°N	115.45°W	25.3	19.3	83°	30.9	0.48
Edouard	14-09-14	09:06	23.97°N	49.82°W	52.3	29.3	12°	25.0	0.51
Simon	14-10-03	13:15	18.38°N	109.47°W	18.4	16.4	60°	32.2	0.56
Phanphone	14-10-04	21:06	28.34°N	131.17°E	72.5	68.5	96°	29.8	0.08
Nuri	14-11-01	20:53	15.09°N	133.00°E	20.0	15.9	111°	33.1	0.33
	14-11-05	20:32	27.67°N	139.72°E	60.8	36.8	29°	29.9	0.47
Vance	14-11-02	01:12	10.25°N	104.87°W	20.6	11.6	169°	18.6	0.14
	14-11-03	13:12	15.00°N	110.65°W	16.2	14.2	79°	40.1	0.45

Table II. Statistics calculated by comparing the wind vector observed by Dropwindsondes and simulated by the two models

	Hurricane Arthur (2014)		Hurricane Earl (2010)	
	Zonal	Meridional	Zonal	Meridional
Number	18	18	6	6
Bias	1.73 m/s	-2.44 m/s	0.18 m/s	-7.43 m/s
RMSE	6.55 m/s	4.82 m/s	13.77 m/s	13.51 m/s
Correlation	91.85%	95.52%	93.21%	96.70%

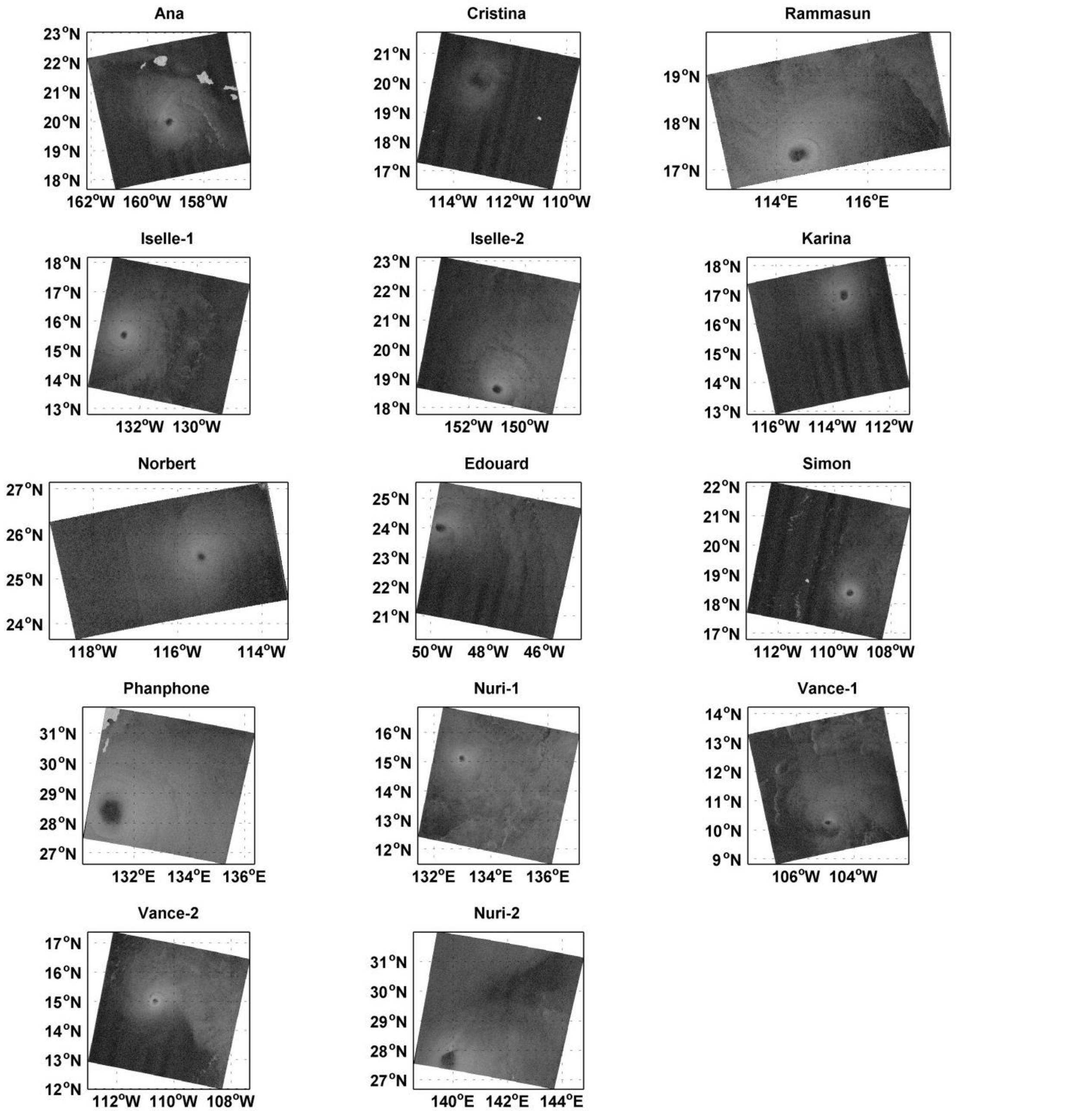

Figure 1. Hurricanes imaged by RADARSAT-2 cross-pol ScanSAR in the year of 2014. The bright spots indicate land.

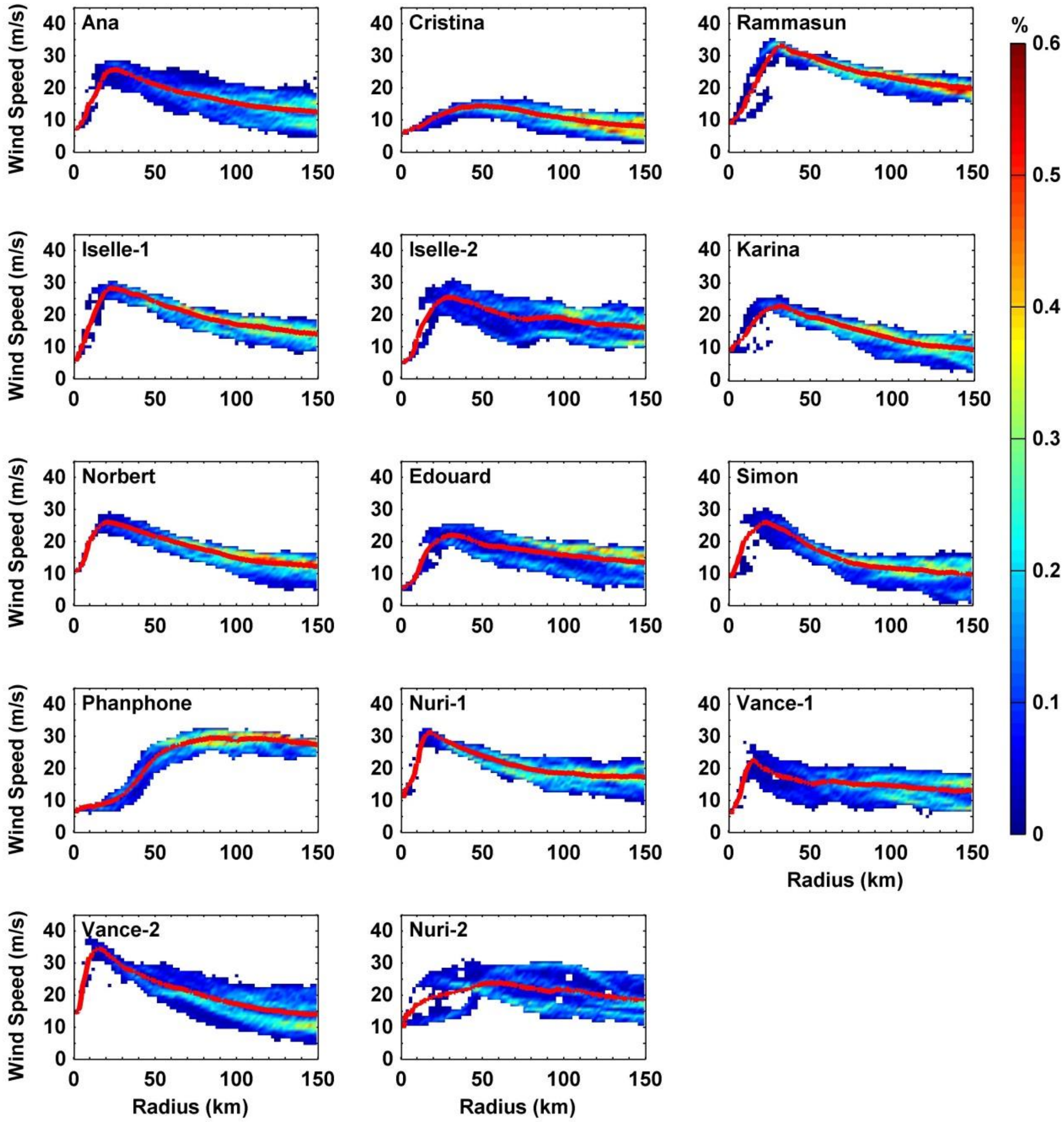

Figure 2. SAR-retrieved wind speed distributions plotted as a function hurricane radius as well as the mean wind profiles in red for the 14 SAR images shown in Fig. 1.

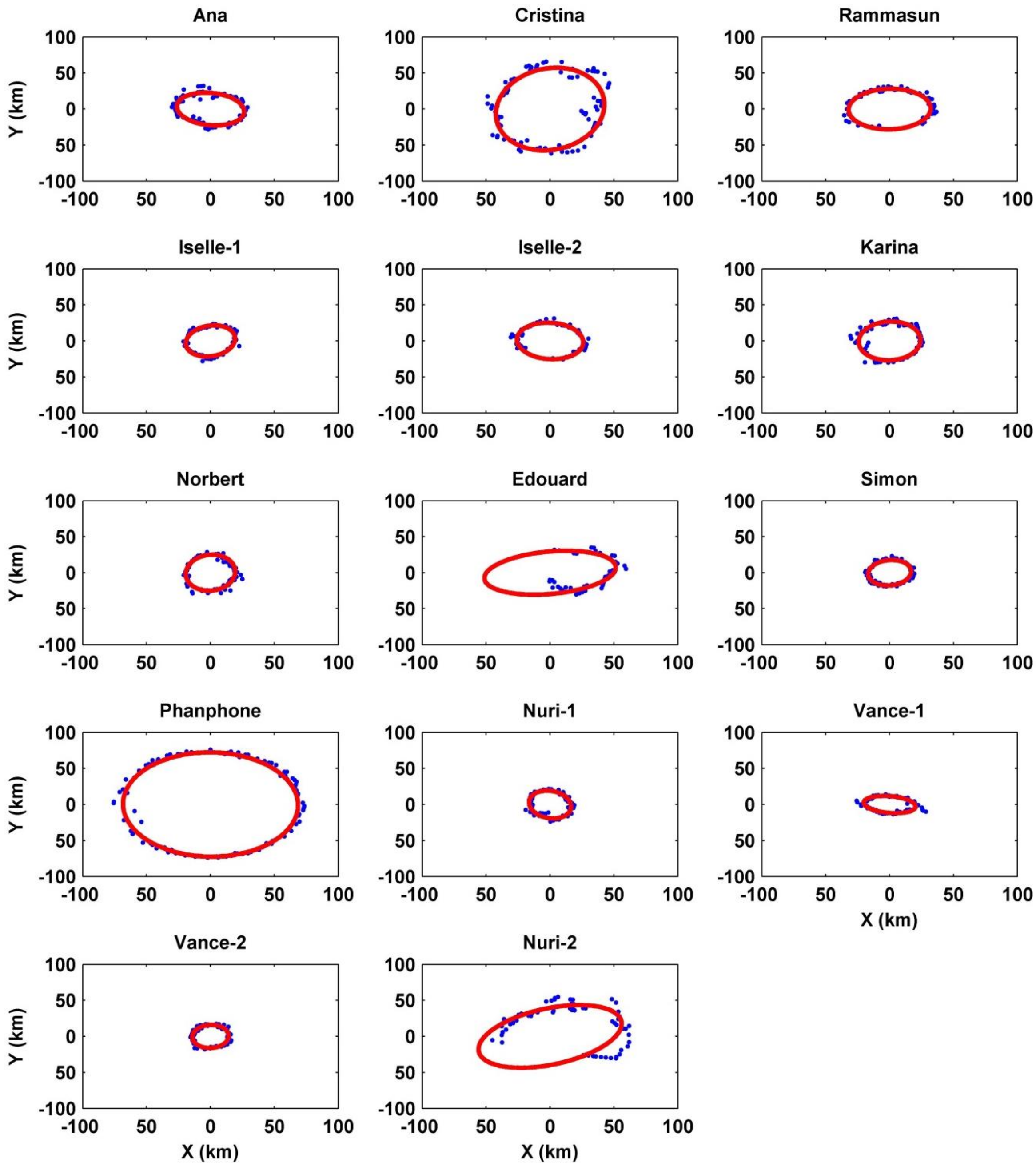

Figure 3. The positions of the maximum wind speed (blue points) derived by the cross-polarization SAR wind speed retrieval algorithm (C-2PO) and the reference ellipse of eyewall (in red) estimated by the SHEW model for the 14 SAR images shown in Fig. 1. The positions of maximum wind speeds were detected for every 5^{o} azimuth angle where the wind speed maxima exist.

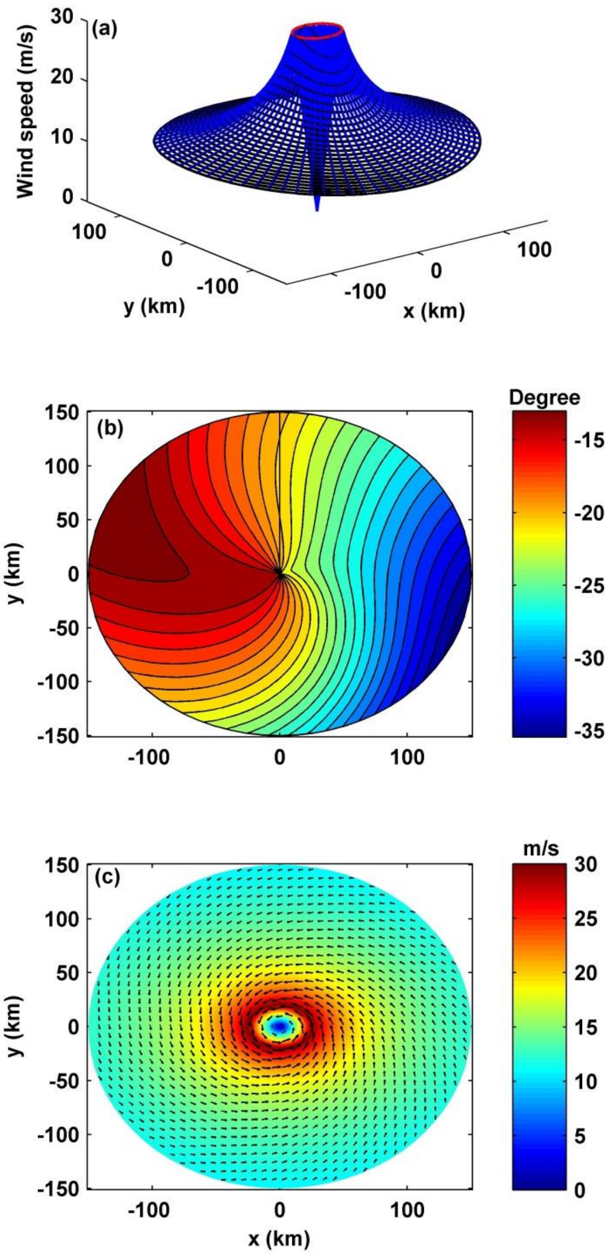

Figure 4. Reconstructed (a) hurricane wind speed by the SHEW model, (b) inflow angle by the revised inflow angle model, and (c) wind vector field estimated by combination of these two models with major axis of 25 km, minor axis of 20 km, the symmetric intensity of 30 m/s, and the hurricane moving speed of 2 m/s toward north.

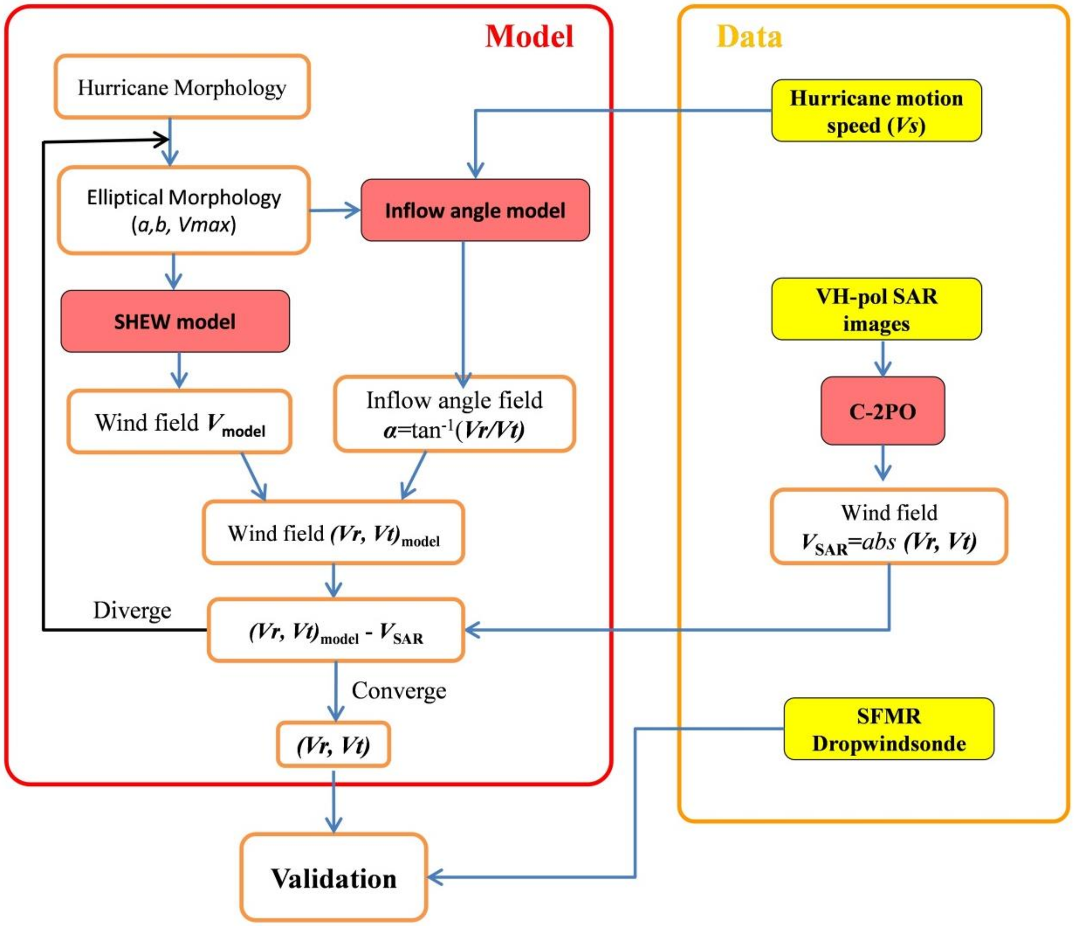

Figure 5. A Flowchart for the combination of the SHEW model and the revised inflow angle model to estimate a complete hurricane surface wind vector field. C-2PO is the cross-polarization SAR wind speed retrieval algorithm.

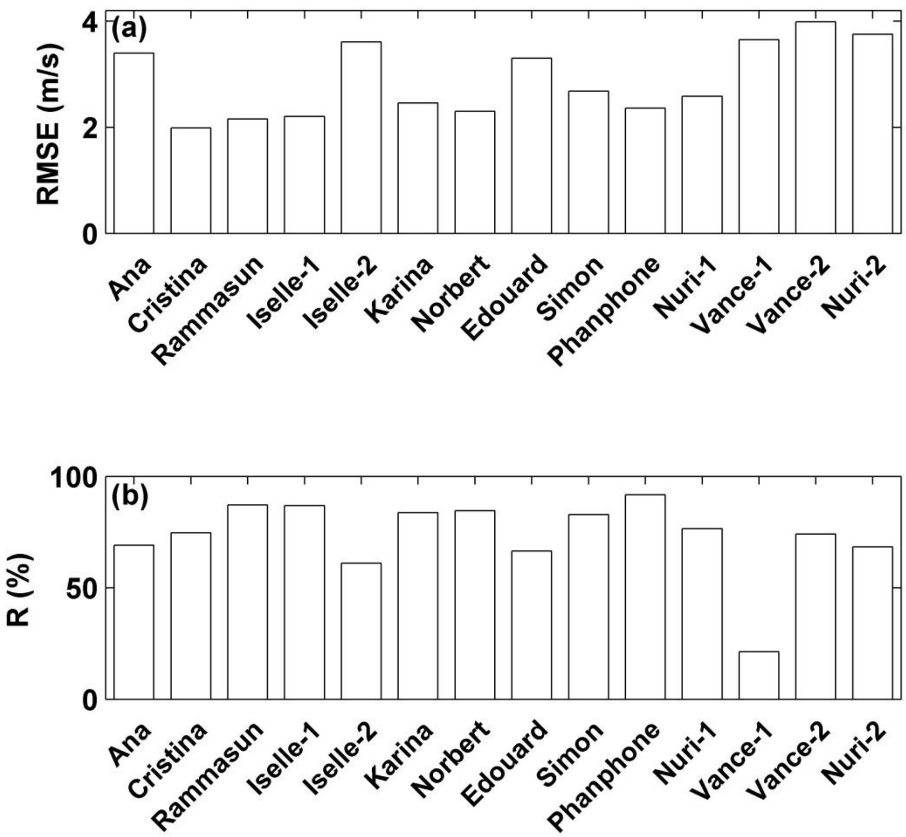

Figure 6. Errors and correlation coefficients between the wind speed derived by the SHEW model and C-2PO SAR algorithm for the 14 SAR images shown in Fig. 1.

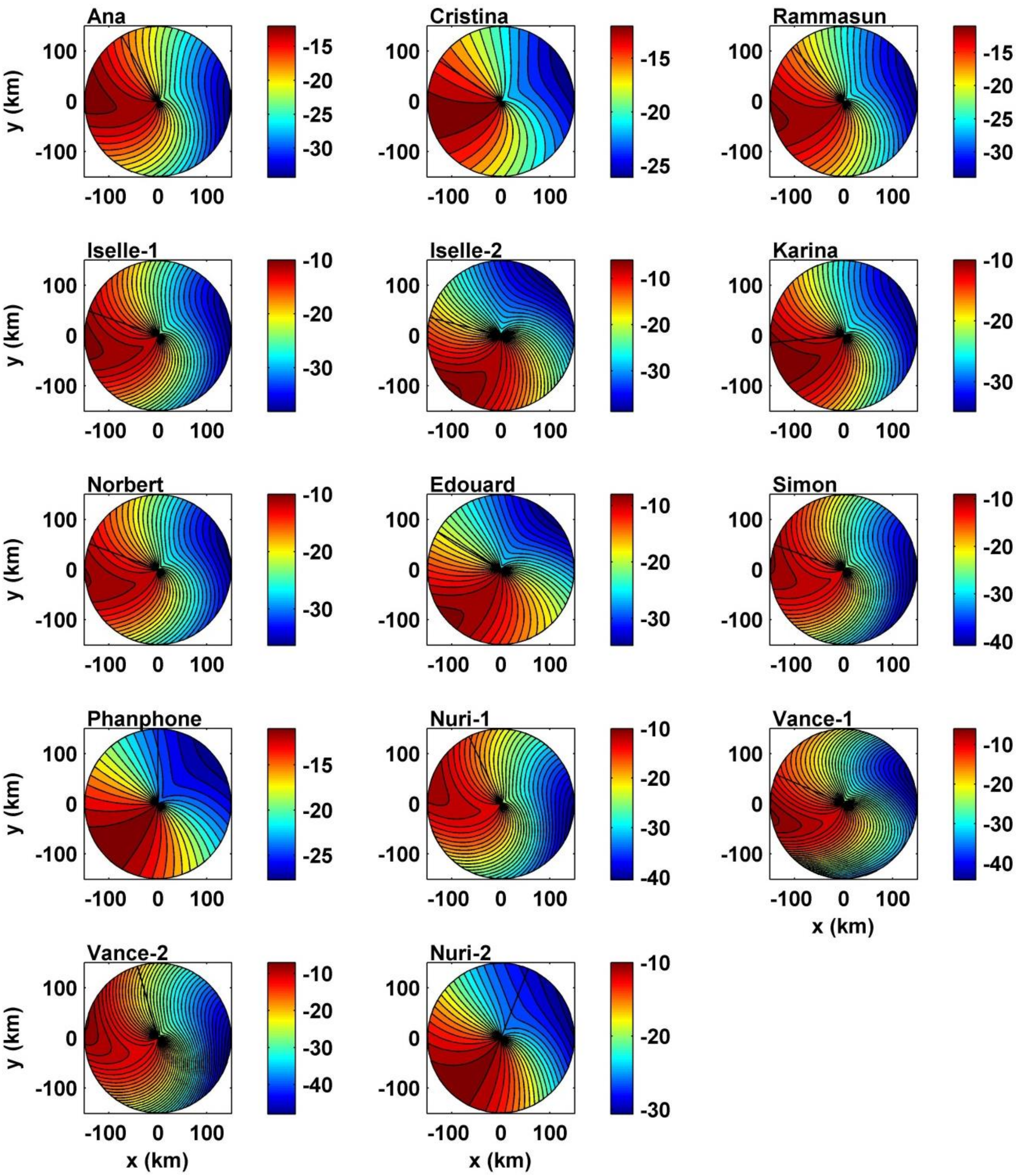

Figure 7. Inflow angle structures estimated by the revised inflow angle model for the 14 SAR images shown in Fig. 1.

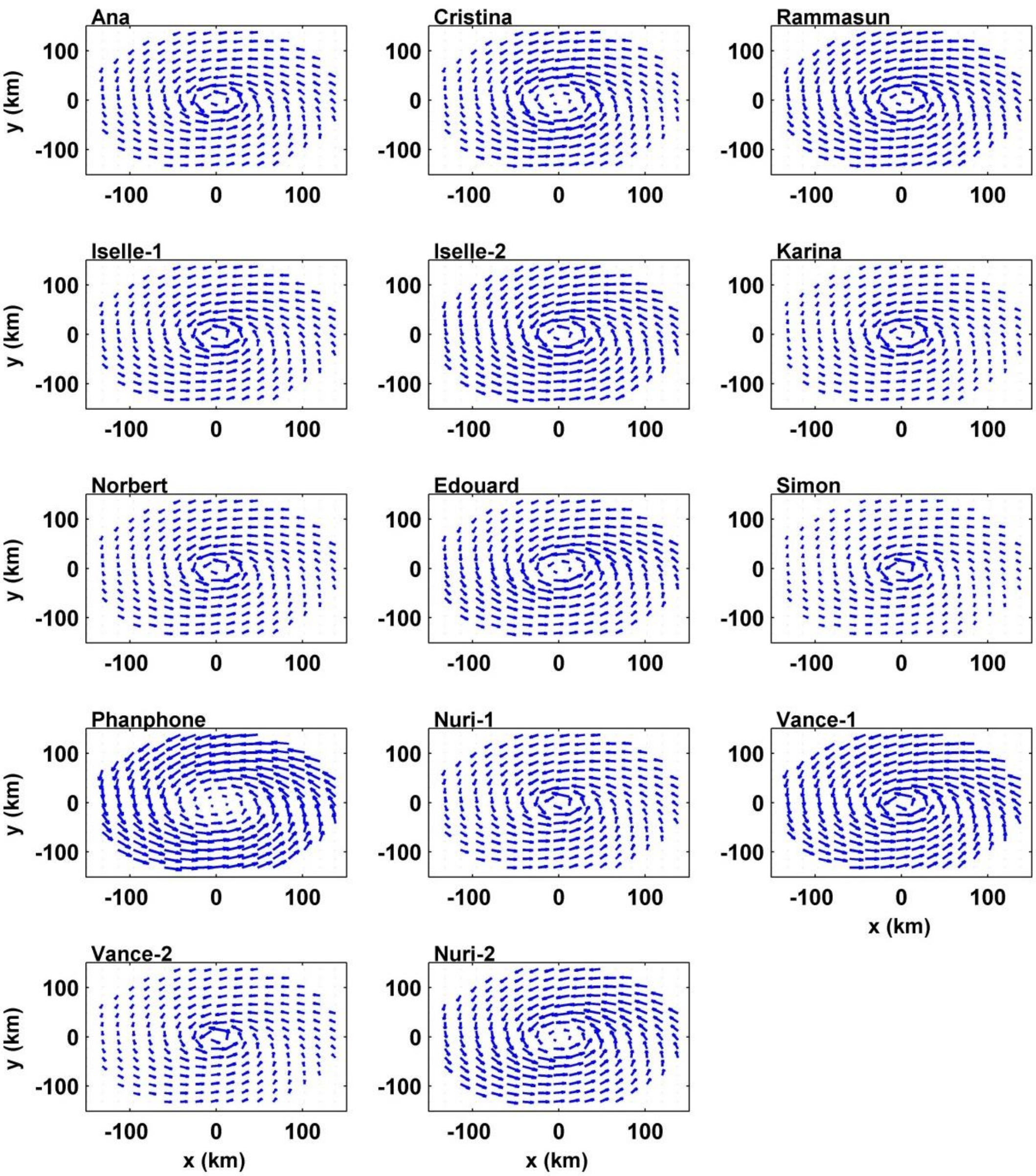

Figure 8. Hurricane surface wind vector estimated by the combination of the SHEW and revised inflow angle models for the 14 SAR images shown in Fig. 1.

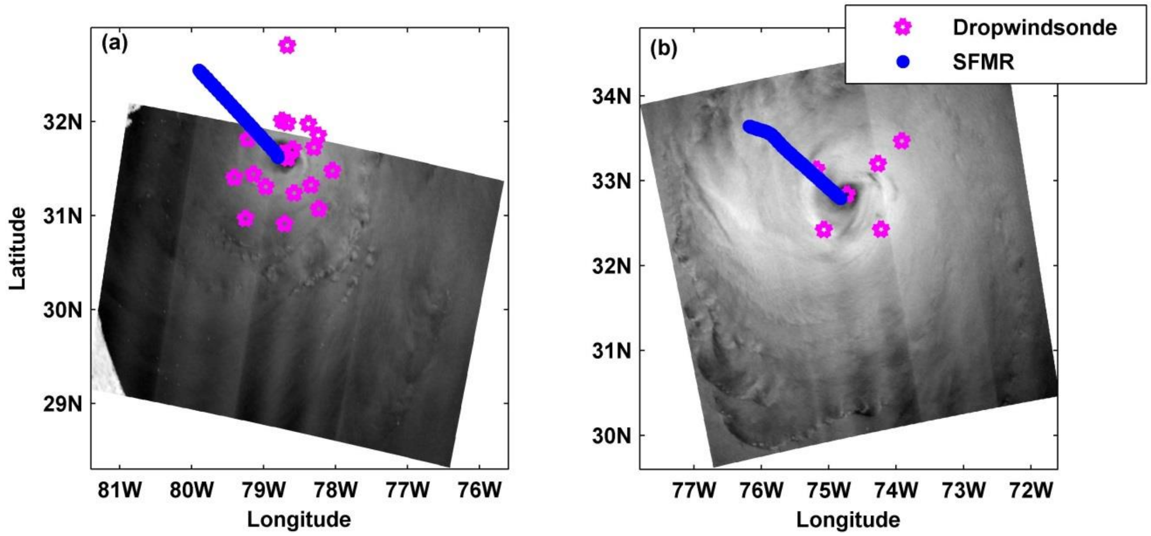

Figure 11. RADARSAT-2 cross-polarized SAR images: (a) Hurricane Arthur (11:14 UTC, July 3, 2014), (b) Hurricane Earl (22:59 UTC, September 2, 2010); the positions of SFMR used here: (a) from 11:04 to 11:27 UTC (July 3, 2014), (b) from 22:59 to 23:19 UTC (September 2, 2010); and the relative positions of the dropwindsondes to the hurricane center during 6 hours of UTC.

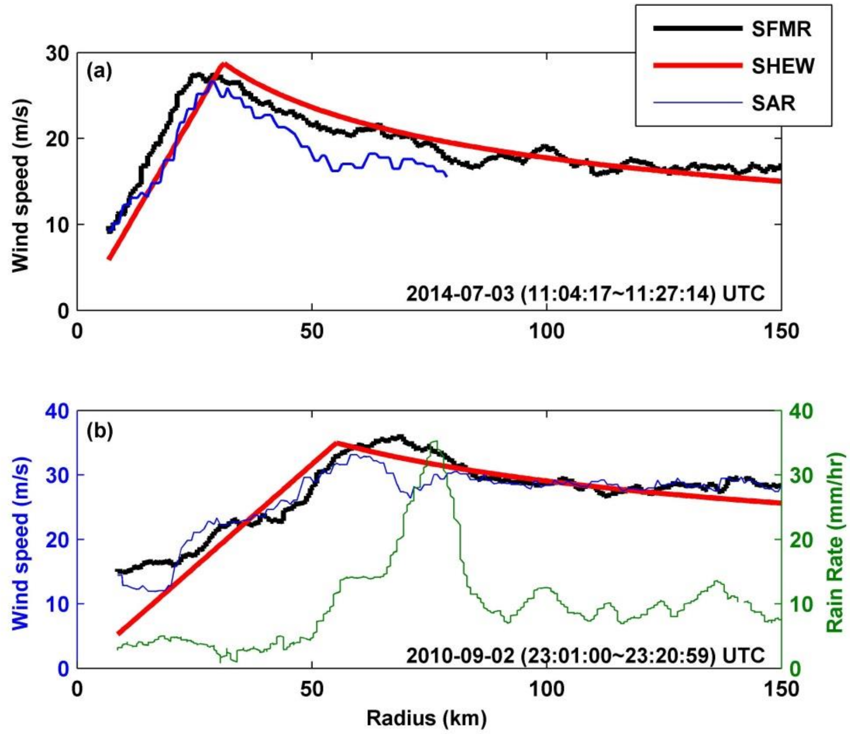

Figure 10. Wind speed profiles measured by the SFMR (black line), estimated by the SHEW model (red line), and retrieved from C-band cross-polarized SAR image using the C-2PO algorithm (blue line) and the rain rate observed by SFMR (green line): (a) Hurricane Arthur (11:14 UTC, July 3, 2014), (b) Hurricane Earl (22:59 UTC, September 2, 2010).

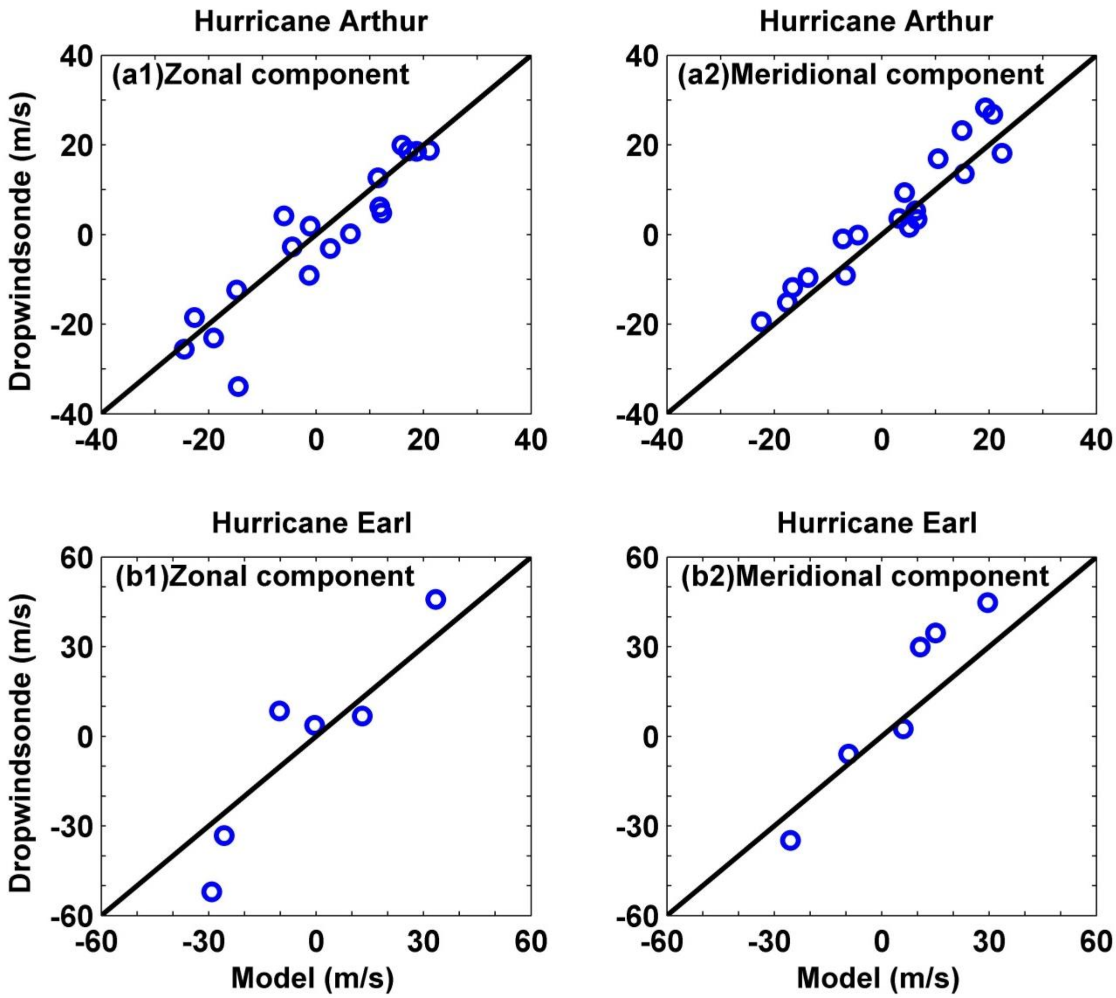

Figure 11. Hurricane wind vector in terms of zonal and meridional components observed by the collocated dropwindsondes compared with that simulated by the combined SHEW and revised inflow angle models: (a) Hurricane Arthur (July 3, 2014), (b) Hurricane Earl (September 2, 2010).